Comparing the micro-vascular structure of cancerous and healthy tissues

Bert Müller*[a], Sabrina Lang[a], Felix Beckmann[b], Marco Dominietto[c], Markus Rudin[c], Irene Zanette[d], Timm Weitkamp[e], Alexander Rack[f], and Simone Elke Hieber[a]
[a]Biomaterials Science Center, University of Basel, c/o University Hospital, 4031 Basel, Switzerland;
[b]Institute of Materials Research, Helmholtz-Zentrum Geesthacht, 21502 Geesthacht, Germany;
[c]Institute for Biomedical Engineering, ETH Zürich, 8093 Zürich, Switzerland;
[d]Department of Physics/Biophysics (E17), TU München, 85748 Garching, Germany;
[e]Synchrotron Soleil, 91190 Gif-sur-Yvette, France;
[f]European Synchrotron Radiation Facility, 38042 Grenoble, France

ABSTRACT

Basic research is required to develop more powerful approaches to prevent, diagnose, and above all to treat cancer, although the clever combination of surgery, chemical, pharmacological, and radiation therapies is well established. Our research activity concentrates on the quantification of the three-dimensional micro-morphology of vessel trees formed in cancerous and healthy tissues of a mouse model *post mortem*. While in several cases it is possible to extract the vessel tree from corrosion casts, phase contrast imaging modalities are needed for cancerous tissues with a significant amount of damaged vessel walls. Differences between cancerous and healthy tissues could be identified. The sum-of-angle metrics is found to be constant for vessel segments in cancerous and healthy tissues with lengths between 12 and 220 μm and corresponds to (0.62 ± 0.10) rad/μm.

Keywords: synchrotron radiation, computed tomography, X-ray phase contrast, sum-of-angle metrics, bifurcation, capillary network, segmentation, vessel endpoints

1. INTRODUCTION

The fight against cancer, one of the most serious diseases and second most frequent cause of death in our developed society, includes prevention, diagnosis and treatment. Although the medical experts cleverly combine more or less established and sophisticated approaches including different kinds of surgery as well as chemical, pharmacological, and a variety of radiation therapies, more basic research is required to develop more effective approaches to prevent, diagnose and treat the various cancerous tissues more successfully. Angiogenesis is one of the most crucial processes that determines growth, survival, and metastasis formation of malignant tumors [1]. Therefore, it is essential to three-dimensionally quantify the anatomy of vessel trees formed in cancerous and healthy tissues. The smaller vessels (capillaries) should be the focus of such studies, as they seem to play a key role during the growth of tumors, which can grow much faster than healthy tissues.

Synchrotron radiation-based micro computed tomography (SRμCT) provides the necessary spatial resolution to visualize the smallest capillaries [2, 3]. The X-ray density resolution obtained using X-ray absorption contrast, however, is too small for segmenting the vessels. While in several cases it is possible to extract the vessel tree from corrosion casts [4], embedded tissues [5] or stained vessels [2, 3], phase contrast imaging modalities are needed for the cancerous tissues, when a significant amount of vessel is damaged [6, 7]. The damaged vessel walls allow penetration of polymer, staining agent or embedding material into the surrounding tissues or vice versa [8]. Such artifacts considerably skew quantities such as bifurcations [9] and have to be avoided. Therefore, X-ray tomography methods based on the phase shifts are much better suited, because they do not require the injection of contrast agents or the application of casting techniques. Although research teams have developed them to a high standard, synchrotron radiation-based phase tomography is not yet as simple to carry out as absorption imaging and requires experienced researchers to extract reliable local refractive indices.

* bert.mueller@unibas.ch; phone +41 61 265 9660; fax +41 61 265 9699; www.bmc.unibas.ch

Developments in X-Ray Tomography VIII, edited by Stuart R. Stock,
Proc. of SPIE Vol. 8506, 850607 · © 2012 SPIE · CCC code: 0277-786/12/$18
doi: 10.1117/12.929941

In the present study, we have applied X-ray phase tomography to quantify the capillary network in tumors of a mouse model. The measurements were complemented by absorption tomography on related casts. To extract the characteristic vessel tree morphology, such as geometry (diameters and lengths), fractal dimension, and bifurcation density, the vessels were successfully segmented and the data had to be converted into vector-based representations [9]. The comparison of these quantities between cancerous and healthy tissues should enable us to identify potential routes in the inhibition of blood supply toward the tumors.

2. MATERIALS AND METHODS

2.1 Specimen preparation

A suspension with 10^6 C51 tumor cells from murine colon carcinoma was subcutaneously injected on the left flank of nude mice (balb/c - Charles River Laboratories, France) in strict adherence to the Swiss law for animal protection and the Declaration of Helsinki. The first mouse was euthanized after seven days and another animal after 14 days. The 7-day old tumor about $(3\ \mathrm{mm})^3$ in size was extracted and fixed in 5% para-formaldehyde solution (PFA) before transfer into the polymer container for SRμCT measurements in phase contrast mode. A polyurethane-based material according to the procedure described by Krucker et al. [4] served for exchanging the blood of the second animal to fabricate a corrosion cast of the entire circulatory system. This cast was fragmented to harvest the tumor vessel tree with a size of about $(10\ \mathrm{mm})^3$ from the left flank and the casted vessels from healthy tissue $(45\ \mathrm{mm})^3$ in size from the right flank of the mouse.

2.2 Data acquisition

Phase contrast-based SRμCT was carried out using the propagation-based technique termed holotomography [10, 11] and conducted at the beamline ID 19 (ESRF, Grenoble, France) [12]. Holotomography relies on phase contrast generated by the propagation of X rays in free space between the tissue specimen and the detection unit. The additional information with respect to the conventional absorption imaging needed to derive the phase was obtained by recording images at different propagation distances. The detector consisted of a 19-μm-thick gadolinium gallium garnet scintillator, microscope optics with 10× overall magnification, and a CCD camera (ESRF FReLoN model 230-42, 2048 × 2048 pixels of 15 μm size), resulting in an effective pixel size of 1.5 μm. Using a photon energy of 17.6 keV, filtered from the undulator spectrum by means of a multilayer, and an exposure time of 0.3 s per radiograph, 800 radiographs for equidistant viewing angles between 0 and 180° were obtained for each of the three specimen-detector distances, which corresponded to 60, 120 and 360 mm. The holotomography data required a phase retrieval procedure prior to tomographic reconstruction. In the following, we shall refer to tomographic reconstruction of phase-retrieved data as 'phase tomography'. The phase retrieval algorithm, implemented in GNU Octave version 2.1.73, was a mixed approach between the contrast transfer function and the transport of intensity equation [13-15].

The tomography data of the cast from the healthy tissue were acquired at the beamline BW 2 (HASYLAB at DESY, Hamburg, Germany). The Institute for Materials Research at the Helmholtz Center Geesthacht, Germany operated the tomography setup [16]. Using a photon energy of 10 keV, a pixel size of 1.98 μm and an exposure time of 5.85 s, 1440 radiographs equidistantly acquired along 360° with an asymmetric rotation axis [17] were combined to 720 radiographs used for data reconstruction. The spatial resolution determined from the 10% value of the modulation transfer function corresponded to 4.7 μm [18]. The X rays were converted to visible light by means of $CdWO_4$ scintillator with a thickness of 200 μm.

Local tomography data of the cast from the cancerous tissue were recorded at the TOMCAT beamline (Swiss Light Source (SLS) at the Paul Scherrer Institut, Villigen, Switzerland) [19] using a photon energy of 15 keV and a pixel size of 0.74 μm and 2× binning, i.e. an effective pixel size of 1.48 μm. The exposure time for each of the 1500 radiographs for equidistant rotation angles between 0 and 180° was set to 0.7 s. The detector with four megapixels covered only around 15% of the cast's projection area.

The tomographic reconstructions were performed using the software tools available at the beamline in DESY, Hamburg [20] based on the conventional filtered back-projection algorithm [21] and using the filtered back-projection technique, implemented in the parallel-beam reconstruction software PyHST (European Synchrotron Radiation Facility, Grenoble, France) [22-24].

2.3 Image analysis

The image analysis of the vascular microstructures was conducted for the absorption tomograms of the cast healthy and cancerous tissues as well as for the phase tomogram of the PFA-fixated tumor tissue. In the case of the corrosion cast it was sufficient to determine an appropriate intensity-based threshold for the segmentation of the vessels from the surrounding air [25].

The phase tomography data were segmented using an implementation of the Frangi-filter in Matlab 7.10.9 R2010a (Simulink, The MathWorks, Inc., USA) [26]. In a second step, the data were skeletonized using a software tool implemented in MS Visual C++ 2010 Express V.4.0.30319RTMRel (Microsoft Corp., Redmond, WA, USA) [27]. For the vector representation of the voxel data we have developed code in Matlab 7.10.9 R2010a [9]. The software VG Studio Max 2.0 (Volume Graphics GmbH, Heidelberg, Germany) served for generating the 3D representations of the vascular microstructures (capillary network) using selected colors.

The center lines of the micro-vessels were extracted using a skeletonization method based on voxel erosion [27]. A 3D-connected component-labeling algorithm was used to sort the skeleton data according to the number of voxels included. The neighboring voxels to each object were determined step-by-step from an arbitrarily selected seed point. We neglected objects with sizes less than 500 voxels and replaced voxels in straight lines with vectors. Finally, the vessel segments were represented as sorted lists of centerline points (vectorization). The components of a vessel included n positions of the vector points r_i, the type of both endings T_1 and T_n (zero means end-point and unity means bifurcation point), its mean radius R_m with the standard deviation R_s and the vessel segment length L. The radii at the centerline points were derived from the distance transform of the tomography data and averaged to R_m. The length L was evaluated by summing up all distances between the vector points.

The tortuosity of the vessel tree was analyzed in terms of the distance metric (DM) and the sum-of-angle metrics (SOAM) [28]. Figure 1 illustrates the meaning of the two quantities in projections. DM corresponds to the ratio of the vessel path length L to the distance between endpoints and bifurcation points T_1 and T_n [29]:

$$\mathrm{DM} = \frac{L}{|T_1 T_n|} \tag{1}$$

Vessels deviating from a straight line showed a distance metric value larger than unity. Since this approach does not distinguish between sinusoidal and C-curved vessels, Bullitt et al. [28] introduced SOAM. This method is based on the ratio between the total curvature of segment and the vessel length, where the total curvature, the integral of the local curvature over the segment, is geometrically interpreted as a sum of the in-plane angle γ_{IP} and the tortuous angle γ_{TP}:

$$\mathrm{SOAM} = \frac{\sum_{k=2}^{n-2}\left(\sqrt{\gamma_{IP,k}^{\ 2} + \gamma_{TP,k}^{\ 2}}\right)}{L} \tag{2}$$

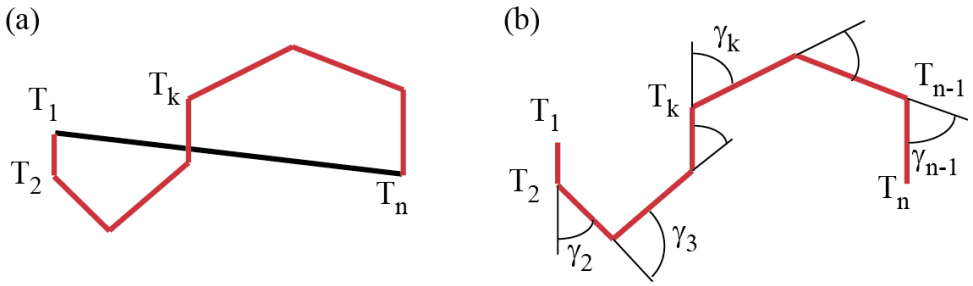

Figure 1. The tortuosity of the red polygonal line can be described using the distance metric DM (a) and the sum-of-angle metric SOAM (b). The distance metric refers to the length of the red line divided by the distance of the end points T_1 and T_n, whereas the SOAM is the ratio of the sum of all angles γ_k with respect to length of the red line.

In case of co-linearity between the two vector points the tortuous angle is defined as zero. In two dimensions the equation simplifies to

$$\mathrm{SOAM} = \frac{1}{L}\sum_{k=2}^{n-1}\gamma_k \tag{3}$$

where γ_k denotes the angle at T_k (see Figure 1 (b)). The results were obtained using every second point of the discretized vessel to reduce misleading effects due to the discretization of the vessel voxel data. The statistical analysis of the SOAM data including the generation of the related diagram was performed by means of the software proFit 6.2.4 (Quantumsoft, Uetikon am See, Switzerland).

3. RESULTS

Figure 2 shows the vectorization of representative capillaries in the cast of the tumor. During the vectorization procedure the centerlines could become interrupted and could lead to neighboring endpoints in the vessel tree as shown in the right upper part of Figure 2. Endpoints should be the exception and only be present at the periphery of the dataset, because the blood flows from the arteries through the capillaries to the veins and back to the heart. This continuous flow is only interrupted in cancerous tissues, which is in an advanced stage of development. A high density of endpoints is therefore an indication for artifacts. Such artifacts may result from the data acquisition and reconstruction or from the data treatment. For that reason, it is highly desirable to carefully analyze the quantities in detail. For example, the number of interruptions in the centerline highly affects the average length of the vessels.

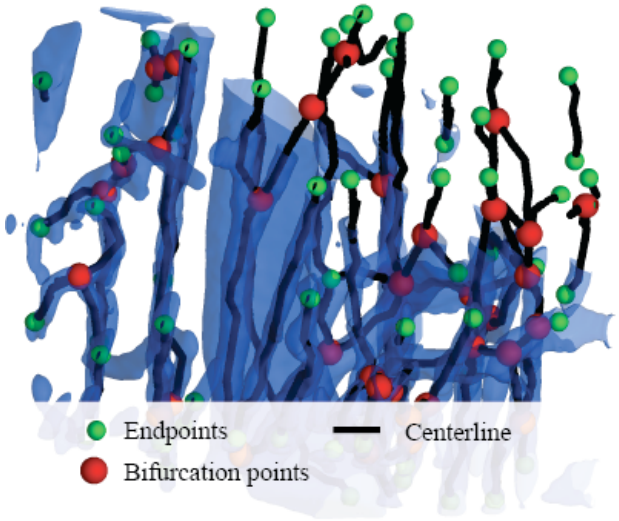

Figure 2. The vectorization of the blood vessels from the tomography, voxel-based data (blue) includes the determination of the centerlines together with their bifurcations and endpoints. The resulting vessel representation as a vector tree allows the straightforward evaluation of characteristic parameters such as bifurcation density and bifurcation angle.

Table 1 lists a selection of derived vessel parameters that not only depend on the type of tissue and to a certain extent on the imaging technique but also on the selected region within the tissue of consideration. The data scattering between the regions of interest are significantly larger than the differences between cancerous and healthy tissues and the differences between the imaging approaches. Therefore, regions larger than $180 \times 180 \times 180$ voxels, i.e. 270 µm × 270 µm × 270 µm, have to be chosen to derive meaningful tissue parameters [9], which allow discrimination between cancerous and healthy tissues.

Another problem relates to the discretization of the voxel-based data, which becomes especially important for smaller vessel segments. In order to demonstrate this phenomenon, we have plotted the relation between SOAM and L for the vessels of the cast from cancerous tissue, cp. open circles in Figure 3. A considerably large amount of short vessels, i.e. about half of the acquired data, have a SOAM value of zero, which is mainly attributed to the discretization procedure of the voxel-based data. As the evaluation of the SOAM in 3D requires at least four points/voxels, vessels with less than eight discretization points do not yield a valid SOAM value. Although vessels with diameters between two and four micrometers are found, it is useless to determine their SOAM. Reasonable values can only be recognized well above L = 12 µm, which corresponds to 8 voxels. The mean SOAM value of the 497 data points above zero corresponds to 0.62 rad/µm (see dashed line). The related median is found to be 0.57 rad/µm. The diagram also shows mean values

within intervals, which are equidistant within the logarithmic length scale for the vessel segments, cp. full circles (SOAM means). The error bars of the averaged SOAM values (SOAM means) correspond to the standard deviations. These error bars illustrate the scattering as the result of variable vessel segment shapes and, especially for the small vessel segments, the steps due to discretization. Therefore, the data close to $L = 20$ µm scatter much more than the data around 100 µm (see Figure 3). The mean SOAM, however, remains constant for all vessel segments detected. It is found to be (0.62 ± 0.10) rad/µm. The identical mean SOAM value was derived for the cast of the healthy tissue. The SOAM values listed in Table 1 are different and have to be handled with care. The numerous short vessel segments with SOAM zero drastically decrease the mean values given in Table 1.

Table 1. Parameters for the vessel cast of the healthy tissue, the one of the cancerous tissue and the vessels from a phase tomography measured tumor at three regions of interests each 180 × 180 × 180 voxels in size.

	Mean diameter [µm]	Vessel length [µm]	Tortuosity		γ_{BIF} [deg]	Vessel volume fraction				Mean void distance [µm]
			DM	SOAM [rad/µm]		3D [%]	2D [%] x	y	z	
Cast, healthy (absorption µCT)	9.0 ± 1.7	15	1.3	0.10 ± 0.17	114 ± 30	7	5	6	7	68.6 ± 2.1
	5.3 ± 0.1	31	1.3	0.10 ± 0.18	116 ± 27	4	4	4	4	71.7 ± 1.2
	0.7 ± 7.3	23	1.2	0.23 ± 0.18	115 ± 25	19	12	12	20	42.2 ± 1.9
Cast, tumor (absorption µCT)	4.0 ± 0.7	20	1.2	0.30 ± 0.20	119 ± 29	7	12	6	6	46.2 ± 2.3
	3.0 ± 1.1	13	1.4	0.28 ± 0.24	114 ± 32	3	2	2	3	43.8 ± 1.4
	3.7 ± 1.0	14	1.3	0.30 ± 0.22	115 ± 29	8	8	13	9	86.1 ± 2.1
Tumor in PFA (phase µCT)	4.8 ± 1.9	12	1.3	0.21 ± 0.27	112 ± 31	2	4	3	4	60.1 ± 2.4
	2.0 ± 2.5	9	1.1	0.23 ± 0.35	107 ± 33	5	3	3	5	76.8 ± 0.8
	6.1 ± 2.6	11	1.3	0.14 ± 0.30	112 ± 33	3	3	2	2	95.1 ± 0.2

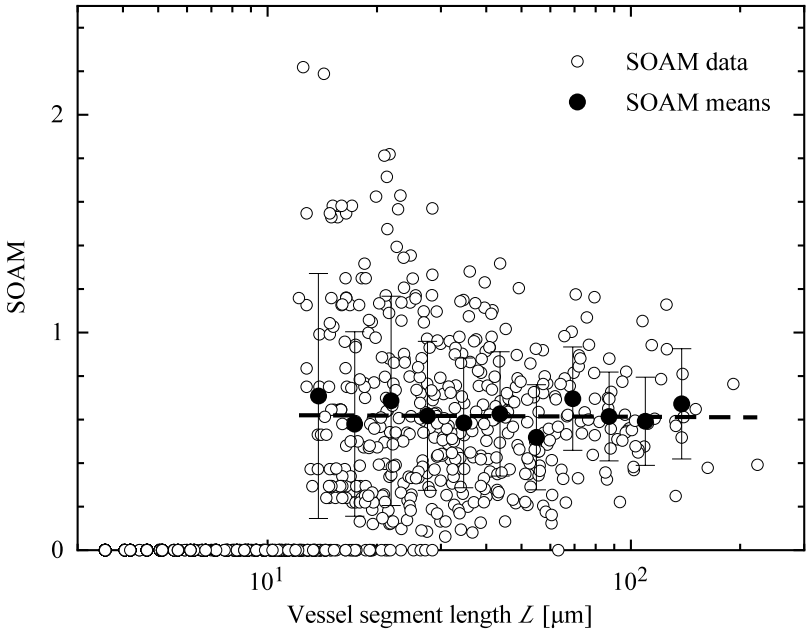

Figure 3. The diagram sum-of-angle-metric (SOAM) given in rad/µm versus vessel segment length L includes more than 1000 vessel segments (open circles). In the selected cast of the cancerous tissue one finds a constant value of 0.62 rad/µm (see full circles and dashed line). This means that SOAM does not depend on the vessel segment length in the range between 12 and 230 µm.

The short vessel segments may come from isolated parts, i.e. capillaries between two endpoints without any bifurcation point. Figure 4 shows the vectorized vessel tree of the holotomography data from cancerous tissue, which contains such 'vessel islands'. They are easily recognized in the periphery, where the vessel density is low. The density of endpoints compared to the density of bifurcation points is surprisingly high and corresponds to a ratio of 1.5. Even for the cast from cancerous tissue measured by means of SRμCT at the Swiss Light Source in absorption contrast mode we have derived this ratio, although the density of vessels is about a factor of three smaller (cp. Figure 5) and isolated capillaries are rare. In both tomography datasets with a size of $(270\ \mu m)^3$ one finds a significant density of endpoints not only at the periphery but also in the center of the tumor located in the central part of the 3D data. The number of endpoints at the periphery is much smaller than the number of endpoints within the region of interest. We have found for the holotomography measurement that 3728 out of 4025 endpoints are within the volume of interest and do not represent intersection points with the surface of the region of interest. For the cast of the cancerous tissue 1253 out of 1481 endpoints are not intersections with the surface of the region of interest. For the measurement of the cast from healthy tissues (cp. Figure 6) these endpoint numbers correspond to 5996 and 6359. It should be mentioned that the endpoint density notably varies within this rather small volume of 180^3 voxels.

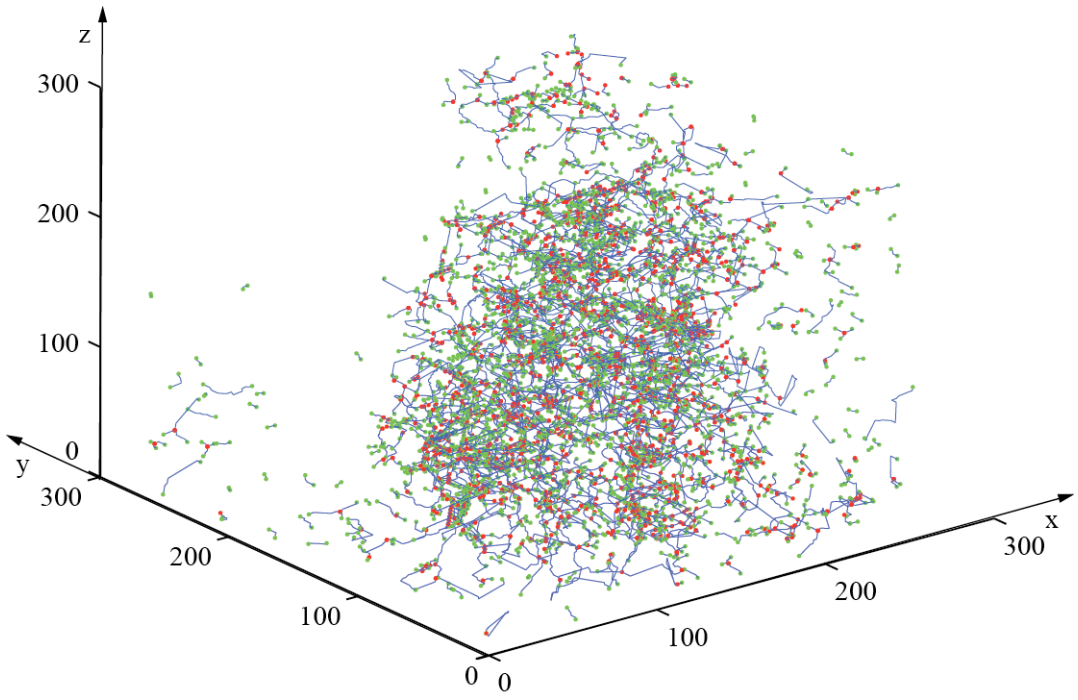

Figure 4. Vector tree of the vascularization based on the holotomography measurement. The detected vessels (blue) are displayed with their 2747 bifurcation points in red and 4025 endpoints in green. The distances from the arbitrarily selected coordinate center are given in micrometers.

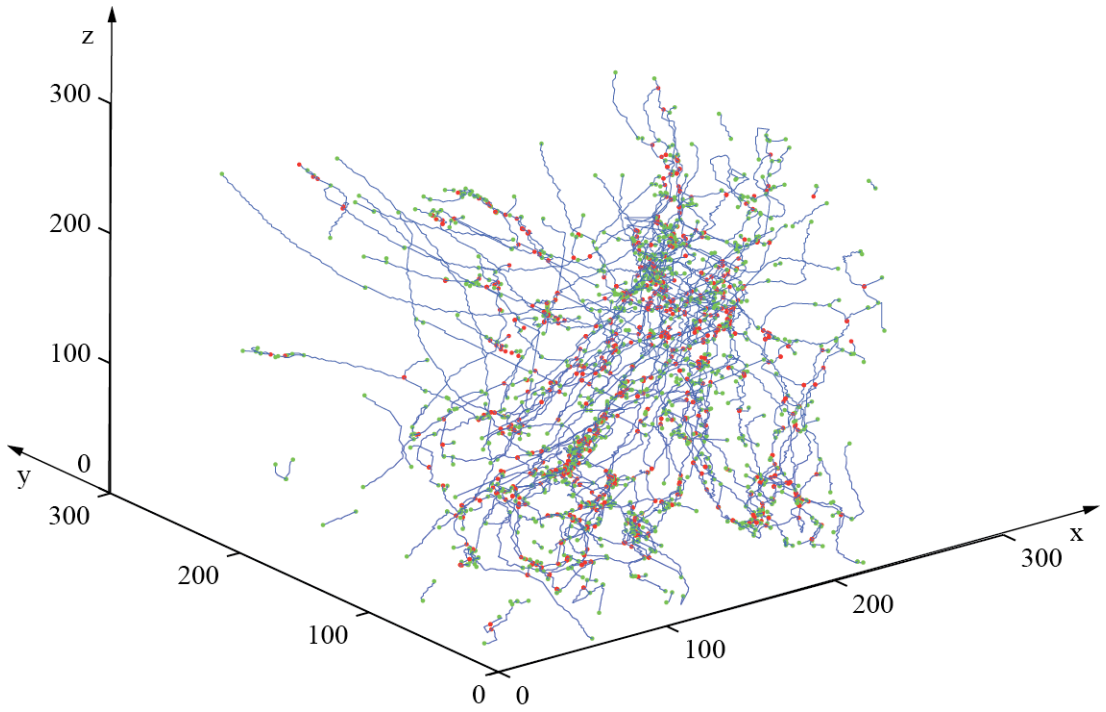

Figure 5. Vector tree of the vascularization from a tumor cast based on the SRμCT measurement. The detected vessels (blue) are displayed with their 1009 bifurcation points in red and 1481 endpoints in green. The distances from the arbitrarily selected coordinate center are given in micrometers.

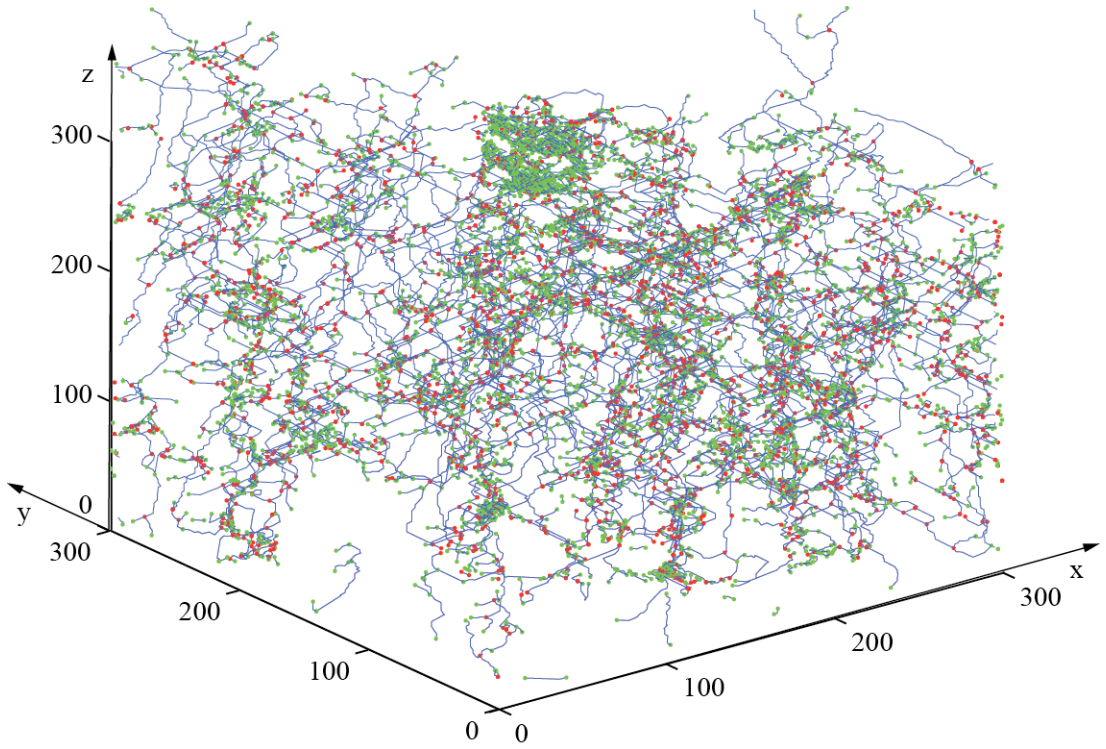

Figure 6. Vector tree of the vascularization from cast healthy tissue based on the SRμCT measurement. The detected vessels (blue) are displayed with their 3835 bifurcation points in red and 6359 endpoints in green. The distances from the arbitrarily selected coordinate center are given in micrometers.

4. DISCUSSION

In mathematical models of the blood flow system, all vessels are connected because they rely on the fact that the blood circulates from the heart via arteries, capillaries, and veins back to the heart. They only exhibit bifurcations but they regularly do not show endpoints. This situation is generally valid for the healthy situation and also a reasonable approximation for tumors. In the final stage, however, tumors become necrotic and endpoints are created, i.e. vessels form that are no longer integrated into the blood flow. Such approaches do not consider the formation of new blood vessels, accommodated with the presence of endpoints.

It is difficult or even impossible to visualize the whole animal or human being using high-resolution SRμCT [30]. Therefore the data are restricted to certain pre-defined volumes termed regions of interest. Vessels will cross the borders of these volumes. These intersections are endpoints. They can be identified using simple procedures and should be eliminated from any quantification, although their number corresponds only to 10% for the rather small regions of interest selected for this study.

Casts of the entire blood vessel system can be fabricated using established preparation procedures. As the polymer replaces the blood, endpoints are usually not created. Therefore, this approach is very helpful for the healthy situation. If the blood vessel system, however, is damaged, i.e. the vessel walls allow the penetration of blood and polymer material, endpoints can be created retrospectively as a result of the preparation procedure. In advanced stages of tumor growth such blood penetration can be observed by the dark red color of the tissue. Also in casts one finds such behavior. Here, additional 'vessels' with endpoints appear, which were never present in the vessel tree. Therefore, the casts of tumors often do not represent the *in vivo* situation.

The data summarized in Table 1 were obtained for three arbitrarily selected regions of interest each 180^3 voxels in size. This size seems to be too small to derive significant differences between cancerous and healthy vessel trees. Comparing, for example, the mean vessel diameters for the cast of the healthy tissue, one finds values ranging from 0.7 to 9.0 μm, i.e. more than an order of magnitude. The mean vessel diameter of 0.7 μm is even lower than the smallest possible diameter of the capillaries. This value is a result of the inappropriate analysis of the small regions fitting the vessel diameter distribution by a Gaussian to determine the average from the maximum as well as the error bars from the full-width-at-half-maximum. Straightforward averaging of the data provides for the three regions of the cast of healthy tissue 9.8, 5.3, and 8.1 μm, respectively. For larger volumes such as $590 \times 590 \times 500$ voxels, however, the Gaussian fitting yields well-defined mean vessel diameters including reasonable error bars, as manually verified. The average difference at 30 locations was approximately 8% between the automatically and the manually determined values [9]. In this manner, it could be demonstrated that the mean vessel diameters of the healthy tissue are two times larger than the capillary diameters in cancerous tissue. The other parameters given in Table 1, i.e. vessel segment length, tortuosity, bifurcation angle, vessel volume fraction, and mean void distance, do not show any significant difference.

Tortuosity is a common parameter used to characterize vessels in cancerous tissue [28]. As the pixel size of about 1.5 μm is close to the diameter of the smallest capillaries, discretization is a crucial issue in the present study. The data represented in the diagram of Figure 3 demonstrate that tortuosity measurements for vessels shorter than 12 μm are meaningless. Between 12 and about 20 μm one only finds discrete tortuosity values, because the number of configurations in voxel-based data is restricted. Since the number of vessel segments in this range, however, is high, averaging leads to well-defined mean tortuosity values. It is not surprising that the tortuosity is constant for vessel segment lengths between 12 and 230 μm, as the curvature per length unit is determined from the vessel formation. This can be, however, significantly different between healthy and cancerous tissues [28]. At first glance, it might be unexpected that vessel segments longer than 200 μm are seldom. It is easily understandable, however, when we consider that diffusive transport of oxygen and nutrients only works to distances of six layers of cells, see e.g. [31]. This is also the reason for the dense capillary network in many tissues of the human body.

Using phase tomography one can avoid the materials-based tissue preparation, i.e. casting, staining, or embedding. Avoiding these time-consuming procedures enables us to perform a wider range of analyses including optical microscopy and histology. It also avoids any preparation-based artifacts in the 3D data. There are, however, also disadvantages, mainly related to higher efforts for data acquisition and data reconstruction as well as reduced spatial resolution or contrast with respect to absorption-based SRμCT of corrosion casts. Therefore, the endpoint density of the phase contrast data we have acquired is about three times larger than the one derived from absorption-based SRμCT. As a consequence, the segmentation procedures should be further improved, e.g. by applying hysteresis thresholding [32]. These improvements will allow us to detect the bifurcation and potential endpoints in the vascular microstructures in

areas of weak contrast or high noise levels (maybe as the result of restricted photon statistics) more reliably than using set fixed thresholds. Capillaries that appear interrupted, for example in the presently available phase tomography data, will be merged to better reproduce the actual situation in the tissues. Furthermore, the phase-based SRμCT techniques with limited spatial resolution such as grating interferometry have to be further developed to reach a spatial resolution of about 1 μm. The phase-based SRμCT techniques with limited contrast for the soft tissues including propagation-based methods have to be improved as well to become a powerful alternative to the absorption-based SRμCT of cast, stained, and/or embedded cancerous tissues.

5. CONCLUSIONS

SRμCT in absorption and phase contrast mode is a powerful technique to visualize the vessel tree of healthy and cancerous tissues. The extraction of meaningful characteristic parameters, however, is not straightforward. First, during the preparation of the tissue, artifacts can be introduced such as partly leaking vessels in polymer casts. Second, the noise within the data as a result of the limited photon statistics for the high-resolution data can lead to vessel interruption or vessel merging. Third, the choice of the segmentation procedure may influence average vessel diameters and lengths. Fourth, the conversion of voxel-based data into vector-based representations gives rise to discrete steps in morphological parameters, which are especially important for small features. Accordingly, the experiments, which include tissue preparation and tomography, as well as the analysis of the large 3D datasets, have to be performed carefully.

In order to understand and influence the cancer-related biological processes such as angiogenesis, many improvements in tissue preparation, high-resolution imaging and 3D data treatments including the extraction of characteristic parameters are required. The presented research project is, therefore, regarded as a seed point for more detailed studies. Here, SRμCT in phase contrast will play a major role.

ACKNOWLEDGMENTS

The authors thank E. Meyer from the Institute of Zoology at the University of Zurich, Switzerland for preparing the corrosion cast of the mouse as well as F. Marone and M. Stampanoni for their active support during the beam time at the Swiss Light Source, Paul Scherrer Institute in Villigen, Switzerland. This basic research project was financially supported by Swiss National Science Foundation grant 200021_127297/1 and in an earlier stage by the National Center of Competence in Research 'Computer-Aided and Image-Guided Medical Interventions' (NCCR Co-Me) of the Swiss National Science Foundation (see http://www.co-me.ch). One of the authors (T.W.) acknowledges support from RTRA 'Digiteo' and RTRA 'Triangle de la Physique' (grants 2009-034T and 2009-79D). Beamtime was granted through the project proposals II 0080040-EC (HASYLAB at DESY, Hamburg, Germany), MD-498 (ESRF, Grenoble, France) and e12159 (SLS at PSI, Villigen, Switzerland).

REFERENCES

[1] R. K. Jain, E. Di Tomaso, D. G. Duda *et al.*, "Angiogenesis in brain tumours," Nature Rev. Neurosci., 8(8), 610–622 (2007).
[2] B. Müller, J. Fischer, U. Dietz *et al.*, "Blood vessel staining in the myocardium for 3D visualization down to the smallest capillaries," Nuclear Instr. Meth. B, 246, 254–261 (2006).
[3] F. Plouraboué, P. Cloetens, C. Fonta *et al.*, "X-ray high-resolution vascular network imaging," J. Microsc., 215, 139–148 (2004).
[4] T. Krucker, A. Lang, and E. P. Meyer, "New polyurethane-based material for vascular corrosion casting with improved physical and imaging characteristics," Microsc. Res. Techn., 69, 138–147 (2006).
[5] B. Müller, M. Germann, D. Jeanmonod *et al.*, "Three-dimensional assessment of brain tissue morphology," Proc. SPIE, 6318, 631803 (2006).
[6] B. Müller, S. Lang, M. Dominietto *et al.*, "High-resolution tomographic imaging of microvessels," Proc. SPIE 7078, 70780B (2008).
[7] B. Müller, G. Schulz, A. Mehlin *et al.*, "Grating-based tomography of human tissues," AIP Conf. Proc., 1466, 107–112 (2012).

[8] S. Lang, M. Dominietto, P.C. Cattin *et al.*, “Global and local hard X-ray tomography of a centimetre-sized tumor vessel tree,” J. Synchr. Rad., 19, 114–125 (2012).
[9] S. Lang, B. Müller, M. D. Dominietto *et al.*, “Three-dimensional quantification of capillary networks in healthy and cancerous tissues of two mice,” Microvasc. Res., in press DOI:10.1016/j.mvr.2012.07.002 (2012).
[10] P. Cloetens, W. Ludwig, J. Baruchel *et al.*, “Holotomography: quantitative phase tomography with micrometer resolution using hard synchrotron radiation x rays,” Appl. Phys. Lett., 75, 2912–2914 (1999).
[11] S. Zabler, P. Cloetens, J.-P. Guigay *et al.*, “Optimizing of phase contrast imaging using hard X rays,” Rev. Sci. Instrum., 76, 073705 (2005).
[12] T. Weitkamp, P. Tafforeau, E. Boller *et al.*, "Status and evolution of the ESRF beamline ID19." AIP Conf. Proc. 1221, 33–38 (2010).
[13] J.-P. Guigay, M. Langer, R. Boistel *et al.*, “Mixed transfer function and transport of intensity approach for phase retrieval in the fresnel region,” Optics Lett., 32, 1617–1619 (2007).
[14] M. Langer, P. Cloetens, J.-P. Guigay *et al.*, “Quantitative comparison of direct phase retrieval algorithms in in-line phase tomography,” J. Med. Phys., 35, 4556–4566 (2008).
[15] M. Langer, P. Cloetens, and F. Peyrin, “Regularization of phase retrieval with phase- attenuation duality prior for 3-D holotomography,” IEEE Trans. Image Process., 19, 2428–2436 (2010).
[16] F. Beckmann, “Microtomography using synchrotron radiation as a user experiment at beamlines BW2 and BW5 of HASYLAB at DESY,” Proc. SPIE, 4503, 34–42 (2002).
[17] B. Müller, R. Bernhardt, T. Weitkamp *et al.*, “Morphology of bony tissues and implants uncovered by high-resolution tomographic imaging,” Int. J. Mat. Res., 98, 613–621 (2007).
[18] B. Müller, P. Thurner, F. Beckmann *et al.*, “Non-destructive three-dimensional evaluation of biocompatible materials by microtomography using synchrotron radiation,” Proc. SPIE, 4503, 178–188 (2002).
[19] M. Stampanoni, A. Groso, A. Isenegger *et al.*, “Trends in synchrotron-based tomographic imaging: the SLS experience,” Proc. SPIE, 6318, 63180M (2006).
[20] F. Beckmann, J. Herzen, A. Haibel *et al.*, “High density resolution in synchrotron-radiation-based attenuation-contrast microtomography,” Proc. SPIE, 7078, 70781D (2008).
[21] A. C. Kak, and M. Slaney, [Principles of Computerized Tomographic Imaging] IEEE Service Center, Piscataway-NJ-USA (1988).
[22] J. Banhart, [Advanced Tomographic Methods in Materials Research and Engineering] Oxford University Press, Oxford (2008).
[23] S. Chilingaryan, A. Mirone, A. Hammersley *et al.*, “A GPU-based architecture for real-time data assessment at synchrotron experiments,” IEEE Trans. Nucl. Sci., 58, 1447–1455 (2011).
[24] A. P. Hammersley, [PyHST: High speed tomography reference manual V0.4], (1999).
[25] B. Müller, F. Beckmann, M. Huser *et al.*, “Non-destructive three-dimensional evaluation of a polymer sponge by micro-tomography using synchrotron radiation,” Biomol. Engin., 19, 73–78 (2002).
[26] D.-J. Kroon, [http://www.mathworks.com/matlabcentral/fileexchange/24409-hessian-based-frangi-vesselness-filter], (2009).
[27] N. D. Cornea, D. Silver, X. Yuan *et al.*, “Computing hierarchical curve-skeletons of 3D objects,” Vis. Comp., 21, 945–955 (2005).
[28] E. Bullitt, G. Gerig, S. M. Pizer *et al.*, “Measuring tortuosity of the intracerebal vasculature from MRA images,” IEEE Trans. Med. Imag., 22, 1163–1171 (2003).
[29] E. M. Brey, T. W. King, C. Johnston *et al.*, “A technique for quantitative three-dimensional analysis of microvascular structure,” Microvasc. Res., 63, 279–294 (2002).
[30] G. Schulz, H. Deyhle, and B. Müller, [Imaging the human body: Micro- and nanostructure of human tissues] Springer, (2012).
[31] B. Müller, M. Riedel, and P. Thurner, “Three-dimensional characterization of cell clusters using synchrotron-radiation-based micro computed tomography,” Microsc. Microanal., 12, 97–105 (2006).
[32] D. Wilson, and J. Noble, "Segmentation of cerebral vessels and aneurysms from MR angiography data," Lecture Notes Comp. Sci., 1230, 423–428 (1997).